This article has been accepted for publication in a future issue of this journal, but has not been fully edited. Content may change prior to final publication. Citation information: DOI 10.1109/TMI.2015.2436711, IEEE Transactions on Medical Imaging

Tissue-dependent and spatially-variant positron range correction in 3D PET.

Jacobo Cal-González, *Student Member, IEEE*, Mailyn Pérez-Liva, Joaquín L. Herraiz, *Member, IEEE*, Juan J. Vaquero, *Senior Member, IEEE*, Manuel Desco, and José M. Udías, *Member, IEEE*.

***Abstract* - Positron range is a significant factor that limits PET image resolution. Its effect is especially relevant with some radionuclides currently used in clinical and preclinical studies such as ^{82}Rb, ^{124}I and ^{68}Ga. The use of an accurate model of the positron range in the image reconstruction holds the potential to minimize its negative impact on the image quality. Nevertheless, positron range distributions are difficult to model, as they may be different at each voxel and direction, depending on the materials that the positron flies through. Several approximated methods have been proposed, considering only one propagating medium (water), or assuming several media without taking into account boundaries effects. In some regions, like lungs or trachea, these methods may not be accurate enough and yield to positron-range artifacts. In this work, we present an efficient method to accurately incorporate spatially-variant positron range corrections in the image reconstruction process for the preclinical Argus PET/CT scanner. The method is based on pre-computing voxel-dependent kernels which take into account at each point and direction the different materials that a positron may travel through until it annihilates. These kernels are obtained from a CT or a manually segmented image, together with a model of the dependence of the positron range on each material derived from Monte Carlo simulations. The images are convolved with these kernels in the forward-projection step of an iterative reconstruction algorithm. This proposed methodology for positron range correction obtains range-corrected and artifact-free images even for large positron range radionuclides (such as ^{124}I) when the activity is concentrated at tissue boundaries with extreme changes of density. The implementation of the algorithm adds a modest overhead to the overall reconstruction time. A full reconstruction for 100 image updates and spatially variant kernel can be obtained in less than 15 minutes by using a parallel implementation in multi-core CPUs. This method can also be applied to other scanners and improve the image quality in clinical PET studies using isotopes with large positron-range.**

***Index Terms*— Nuclear imaging (PET), Image reconstruction - iterative methods, Positron range correction**

I. Introduction

SINCE the last two decades, alternative radionuclides with large positron range (PR), such as ^{68}Ga, ^{82}Rb or ^{124}I have been proposed for Positron Emission Tomography (PET) imaging. The National Institute of Health (NIH) molecular imaging and contrast agent database[1] lists almost 800 molecular imaging radiotracers with potential clinical and preclinical applications [1], and the use of these radiotracers is clearly increasing within the last years. However, the use in PET of radionuclides with large PR raises questions about their ability to provide images of good quality and accurate quantification. At a local level, PR appears as an additional blurring on the reconstructed image. The extent of the blurring depends on the positron kinetic energy spectrum of the radioisotope (larger range for higher energies), and on the underlying tissue densities (larger range for low electron densities). Furthermore, PR may induce not only a blurring on the images, but also some artifacts due to the incorrect redistribution of the activity in a large and inhomogeneus volume. Therefore, in order to obtain optimal PET images, an accurate estimation and correction of PR for every specific isotope and propagation material is needed [2,3]. This correction should take into account the possibly large PR in low-density regions like the air or the lungs.

A number of studies have shown that accurate modeling of the physical effects related to the emission and detection of the

Manuscript received March 11, 2015; revised May 13, 2015; accepted May 17, 2015. "This work was supported by Comunidad de Madrid (S2013/MIT-3024 TOPUS-CM), Spanish Ministry of Science and Innovation (grants FPA2010-17142, FPA2013-41267, ENTEPRASE PSE-300000-2009-5), by European Regional Funds: Human Frontier Science Program grant RGP0004/2013, by CPAN: CSPD-2007-00042@Ingenio2010 and by the Innovative Medicines Initiative Joint Undertaking under grant agreement no. 115337, which comprises financial contributions from the European Union's Seventh Framework Programme (FP7/2007-2013) and EFPIA companies' in kind contribution. Part of the calculations were performed in the "Clúster de Cálculo de Alta Capacidad para Técnicas Físicas" funded by UCM and by UE under the FEDER programme." The associate editor coordinating the review of this manuscript and approving it for publication was Prof. Xiaochuan Pan. *(Corresponding author: J. Cal-Gonzalez)*

J. Cal-Gonzalez was with the Grupo de Física Nuclear, Dpto. Física Atómica, Molecular y Nuclear, Universidad Complutense de Madrid, CEI Moncloa, Madrid, Spain. He is now with the QIMP group, Center for Medical Physics and Biomedical Engineering, MUW, Vienna, Austria (e-mail: jacobo@nuclear.fis.ucm.es).

M. Perez-Liva, J.L. Herraiz and J.M. Udias are with the Grupo de Física Nuclear, Dpto. Física Atómica, Molecular y Nuclear, Universidad Complutense de Madrid, CEI Moncloa, Madrid, Spain.

J. L. Herraiz is also with Madrid-MIT M+Visión Consortium, Research Lab. of Electronics, Massachusetts Institute of Technology, Cambridge, MA, USA.

J. J. Vaquero and M. Desco are with Departamento de Bioingeniería e Ingeniería Aeroespacial, Universidad Carlos III de Madrid, Spain.

M. Desco is also with Instituto de Investigación Sanitaria Gregorio Marañón, Madrid. CIBERSAM, Madrid, Spain.

Digital Object Identifier xx.xxxx/TMI.2015.xxxxxxx

[1] MICAD. Molecular imaging and contrast agent database, http://www.ncbi.nlm.nih.gov/books/NBK5330/.

This article has been accepted for publication in a future issue of this journal, but has not been fully edited. Content may change prior to final publication. Citation information: DOI 10.1109/TMI.2015.2436711, IEEE Transactions on Medical Imaging

radiation in the reconstruction of PET data lead to superior image quality [4-7]. For this reason, modeling of positron physics, such as PR and photon non-collinearity has attracted growing attention in the last years [4,5].

The blurring effects of PR have been measured for several radionuclides of interest in medicine [8-10]. Nevertheless, these experiments had limited accuracy because the resolution of the detector was comparable to the PR measured. For that reason, other authors proposed to compute range distributions using analytical formulae [11-13], or by means of Monte Carlo simulations [14-23]. According to these studies, the blurring introduced by PR in water goes from a few tenths of a millimeter for lower-energy emitters to several millimeters for higher-energy radionuclides.

Several correction approaches have been proposed to remove the blurring caused by PR. One of the most straightforward techniques is Fourier-deconvolution [24]. The main downside of this estimation lies in its disregard of the tissue where positrons annihilate. This results in over- or infra-corrected images if positron annihilations take place in a non-water equivalent tissue, such as the lungs or bones. Other approaches, which used material-dependent space-invariant isotropic filters, obtained from a CT or MRI anatomical image, have been also proposed to deconvolve the positron-range effect with a blurring kernel [25-27]. These approaches are computationally efficient and valid for cases in which the activity is within a homogeneous medium. However, in small-animal PET studies, a non-negligible amount of positrons emitted near to the air boundary can travel a long distance, violating the space-invariant assumption. Thus, using space-invariant deblurring filters can result in non-negligible artifacts [28], [29]. Boundaries between lung/soft tissue and tissue/bone may lead to similar effects.These artifacts were also observed, in clinical ^{124}I PET imaging of thyroid glands near to the trachea [30].

To address inhomogeneous media, space-variant analytic filtering approaches were proposed. Bai and collaborators [28, 29] compensated for variant PRs by either A) anisotropically truncating an isotropic point probability density function dependent on tissue type, or B) performing successive convolution operations of tissue dependent range kernels to determine range models across tissue boundaries. On the other hand, Alessio and MacDonald [31] averaged the fitting parameters of the 1D annihilation densities for originating and target voxels. These filters may be a fast and robust method for implementing PR correction, but due to the complexity of positron migration at irregular interfaces, developing such filters is usually difficult and may be not always accurate.

An alternative to analytical models is the use of Monte Carlo (MC) simulations [32], which are able to model complex structures of biological tissues if sufficient details about the attenuation media are available. However, MC simulations are also associated with long computational times [32]. To solve this problem, Fu et al [33] proposed a MC-based PR model to be incorporated into a factorized system matrix in high-resolution MAP-OSEM image reconstruction. Alternatively, Krauss et al [26] developed MC-based correction kernels for PR in the presence of magnetic fields. They also presented a generalized method able to reduce the amount of wrongly allocated activity using pre-simulated datasets incorporating tissue borders. This method worked well in water-lung boundaries, but extensions to more tissue types and multiple tissue borders would increase the database significantly.

In this work, we present a new full PR correction method for PET imaging, that is both accurate and computationally efficient, and show results with the preclinical Argus PET/CT scanner [34]. To make the implementation useable in a reasonable time, we used an analytical expression for the PR blurring kernel as a function of the total density transversed, obtained from fits to Monte Carlo simulations of PR [15] for several radioisotopes and materials. The procedure fully takes into account the different materials that the positron travels by until it annihilates; the material distribution information is taken from a CT or segmented images. This kernel is employed during the forward projection step in the iterative reconstruction procedure without a significant impact on the overall computational time. To evaluate the effect of the full PR correction, as compared to simplified approaches, two alternatives have been evaluated:

- Tissue-dependent correction with homogeneous, isotropic kernel (TD-PRC): the blurring kernel depends on the voxel to which is applied, that is, the blurring kernel is taken from the material where the positron is emitted, irrespectively of the surrounding media. The blurring is thus homogeneous and isotropic. This correction needs the co-registration of the CT image and is expected to work well everywhere except near tissue boundaries.
- Tissue-dependent and spatially-variant correction (TDSV-PRC): the blurring kernel takes into account not only the material at which the positron is emitted but also the different materials that the positron travels by until it annihilates. This approach should be realistic enough even when the activity is concentrated at tissue boundaries with extreme changes of density.

II. Materials and Methods

A. Positron range modelling

PR distributions for the most common radionuclides used in PET were obtained using Monte Carlo simulations with PeneloPET [35]. PeneloPET is built on top of PENELOPE [36] (version 2008 [37]) and provides a simple framework to simulate PET scanners. PeneloPET is freely available and can be obtained under request[2].

In [15] we demonstrated that, for radionuclides that emit positrons with only one maximum energy, or with two very similar ones, the radial integrated range distribution (*g3D(r)*) obtained from the simulations can be modeled by the following analytical expression:

$$g_{3D}(r) = C\left[(a \cdot r + 1)\left(1 - \frac{r}{r_0}\right)^n - \frac{\varepsilon}{(r)^n}\right] \quad (1)$$

[2] see http://nuclear.fis.ucm.es/penelopet

This article has been accepted for publication in a future issue of this journal, but has not been fully edited. Content may change prior to final publication. Citation information: DOI 10.1109/TMI.2015.2436711, IEEE Transactions on Medical Imaging

where a, r_0, n and ε are fitting parameters, and have been obtained using a genetic algorithm [15]. C is a constant employed to scale g_{3D} to the data and r_0 represents the maximum PR.

In the case of multiple positron-emitting radionuclides (as for example ^{76}Br and ^{86}Y), expression (1) does not fit well $g_{3D}(r)$, due to the fact that there are many positron emissions with different maximum energies and similar probabilities. For the multiple positron-emitting radionuclides, we modeled $g_{3D}(r)$ using:

$$g_{3D}(r) = C\left[A_1 \cdot r \cdot e^{-\frac{(r-B_1)^2}{C_1}} + A_2 \cdot e^{-\frac{(r-B_2)^2}{C_2}}\right]\left[1-\left(\frac{r}{r_0}\right)^2\right] \quad (2)$$

for r < r0 , and zero otherwise. A_1, B_1, C_1, A_2, B_2, C_2, r_0 and n are the fitting parameters. Expression (2) has three parts: first term (Gaussian function multiplied by r) represents the contribution to range of positrons emitted at low energies; the second term (Gaussian function) represents the contribution of high energy cascades. Finally, in the third part of the equation, the r_0 fitting parameter, as in (1), represents the maximum PR.

The fitting parameters for the radionuclides included in our reconstruction algorithm are presented in tables I and II.

To obtain material-independent profiles, a scaling by the density of material was performed, as explained in [15]. This is a good approximation at the energies involved, as the Linear Energy Transfer (LET) of electrons/positrons scales well with the electronic density of the material. The use of this scaling is a critical step in the method, as it allows us to use an universal PR curve for each radionuclide, derived from simulations in water. To introduce tissue-scaling to compute the blurring kernel for other biological tissues, we just scale the universal PR profile by the tissue density, without the need of computing the PR distribution for each tissue, paving the way for fast algorithms to correct images for PR during reconstruction.

B. Tissue-dependent positron range correction

Positron range correction was performed by using the positron range profiles obtained from Monte Carlo simulations as an additional blurring applied to the image.

The System Response Matrix (SRM) was simulated using PeneloPET [35] without positron range effects, but considering all other physical effects such as non-colinearity or inter-crystal scatter. Following a similar approach as in [38] the tissue-dependent spatially-invariant PR corrected OSEM (PR-OSEM) algorithm reads:

$$x_j' = x_j \frac{\sum_i A_{ij}\left(\frac{y_i}{\sum_j A_{ij}\tilde{x}_j}\right)}{\sum_i A_{ij}} \quad (3)$$

where $\tilde{x}_j$ is the image blurred by PR that is forward projected. $\tilde{x}_j$ is obtained by the filtering of the initial image with a blurring function corresponding to the annihilation Point Spread Function (aPSF) range profile of the emitter present at voxel j:

$$\tilde{x}_j = x_j \otimes aPSF = \frac{\sum_{j'} x_{j'} \cdot aPSF(r_{eq}^{jj'})}{\sum_{j'} aPSF(r_{eq}^{jj'})} \quad (4)$$

where the filtering is extended to all the *j'* neighboring voxels of *j*, $x_{j'}$ is the activity of the initial image in voxel *j'*, and $aPSF(r_{eq}^{jj'})$ is the value of the aPSF with origin in *j*, at voxel *j'*. $r_{eq}^{jj'}$ is the distance from *j* to *j'*, scaled to equivalent distance in water, using as reference the tissue in *j*. $aPSF(r_{eq}^{jj'})$ can be obtained from the g_{3D} analytic distribution using:

$$aPSF\left(r_{eq}^{jj'}\right) = \frac{g_{3D}(r_{eq}^{jj'})}{\left(r_{eq}^{jj'}\right)^2} \quad (5)$$

and $r_{eq}^{jj'}$ is given by:

$$r_{eq}^{jj'} = r^{jj'} \cdot \rho_j \quad (6)$$

where $r^{jj'}$ is the geometrical distance between voxels j and *j'* and ρ_j is the density at voxel *j*. It is this dependence in the density explicit in (6) which contains the tissue dependence of the procedure. The kernel to include PR is computed only once, from the external image providing the density information, and then it is applied during the projection stage of the image reconstruction.

TABLE I. PARAMETERS OF THE FIT TO THE G_{3D} DISTRIBUTION OF PENELOPET TO EQ. (1) FOR $5\cdot10^6$ POSITRONS ANNIHILATING IN WATER. THE PARAMETER $\mathbf{r_i}$ IS DEFINED AS: $r_i = \varepsilon/(r)^n$

Radionuclide	a (mm^{-1})	r_0 (mm)	n	r_i (mm)
^{18}F	2.60	2.39	4.04	0.051
^{11}C	1.48	3.80	3.16	0.21
^{13}N	1.46	4.95	3.04	0.29
^{15}O	1.15	7.90	3.09	0.36
^{68}Ga	2.41	8.98	3.27	0.20
^{124}I	3.07	11.0	4.46	0.36
^{94m}Tc	2.49	11.1	2.72	0.33
^{82}Rb	7.13	16.6	3.11	0.41

TABLE II. PARAMETERS FOR THE FIT OF G_{3D} DISTRIBUTION TO EQ. (2) FOR $5\cdot10^6$ POSITRONS ANNIHILATING IN WATER.

Radionuclide	A_1 (mm^{-1})	B_1 (mm)	C_1 (mm)	A_2	B_2 (mm)	C_2 (mm)	r_0 (mm)	n
^{76}Br	9.40	-3.26	7.27	0.52	5.74	35.5	21.8	1.48
^{86}Y	12.5	-3.07	13.1	0.39	6.00	16.9	14.7	0.12

This article has been accepted for publication in a future issue of this journal, but has not been fully edited. Content may change prior to final publication. Citation information: DOI 10.1109/TMI.2015.2436711, IEEE Transactions on Medical Imaging

The factor $\sum_{j'} aPSF(r_{eq}^{jj'})$ in (4) is included in order to normalize the number of counts after the blurring operation; that is, the number of counts in the blurred image must be the same than in the initial image. As it can be noticed, a mis-matched projector / backprojector pair is used in (2). Indeed, PR blurring is only applied in the forward projection operation. This approach has been used in several works [39], [40], and it has been shown that good reconstructed images can be attained with a full modeling of blurring effects during the projection step, whereas a simplified modeling is employed in the backprojector [25]. We have also seen that the main effect of using a detailed range blurring kernel in the backprojector is reducing the convergence speed of the iterative algorithm [25].

C. Spatially-variant positron range correction

In non-homogenous tissues, accurate positron range modeling requires anisotropic kernels, which ideally would be derived from Monte Carlo simulations for each tissue distribution. This can be computationally very intensive. Thus, a primary challenge in determining the range effect in non-homogenous media is how to model the range across boundaries in an efficient way. In this work we propose a simple but accurate method to correct for PR in heterogeneous media (see Fig. 1A). First, we automatically generate a segmentation of the CT image (as it was previously mentioned), to find the boundaries between tissues. For each voxel j of the image, we determine whether there is any boundary close to that voxel, at a distance smaller than the kernel size, scaled to the actual material of the voxel, used to blur the image. If not, the voxel is marked so that any emission from it will be blurred with a homogeneous kernel (as in the previous section) adequate to the material. Otherwise, the voxel goes to the list of voxels to compute the blurring kernel in a realistic way, taking into account the different densities of every material surrounding the voxel. To this end, for each target voxel j_0 of the blurring kernel we obtain the densities of the voxels associated with the line connecting the originating voxel j and the target voxel j_0 (see Fig. 1A).

To compute the water-equivalent distance between j and j_0 a scaling by the mean density of all the voxels associated with the line connecting the originating voxel j and the target voxel j_0 is employed. The average density (ρ_m) is calculated from:

$$\rho_m = \sum_{n \in L(j,j')} \frac{\rho_e^{(n)}}{N} \qquad (7)$$

Where *L(j,j')* is the line connecting the voxels *j* and *j'*, N is the total number of voxels associated with *L(j,j')* and $\rho_e^{(n)}$ is the electronic density of each voxel. The water-equivalent distance $r_{eq}^{jj'}$ between *j* and *j'* is now given by:

$$r_{eq}^{jj'} = r^{jj'} \cdot \rho_m \qquad (8)$$

Where $r^{jj'}$ is the geometrical distance between j and *j'* and ρ_m is the mean density obtained from (7). Using this procedure we obtain a blurring kernel $g_{3D}^{(j)}$ for each voxel *j*. This kernel may be homogeneous, if there are not tissue-boundaries within the spatial extent of the kernel, or inhomogeneous if there are tissue boundaries within the kernel volume. As mentioned before, these blurring kernels are computed at the beginning of the PET reconstruction, once the CT image was obtained. Finally, the blurrring for each voxel j is computed using expression (4) and the blurring kernel obtained for the corresponding voxel. In Fig. 1B we present the homogeneous and spatially-variant blurring kernels for a case in which the activity is located near to an air cylinder.

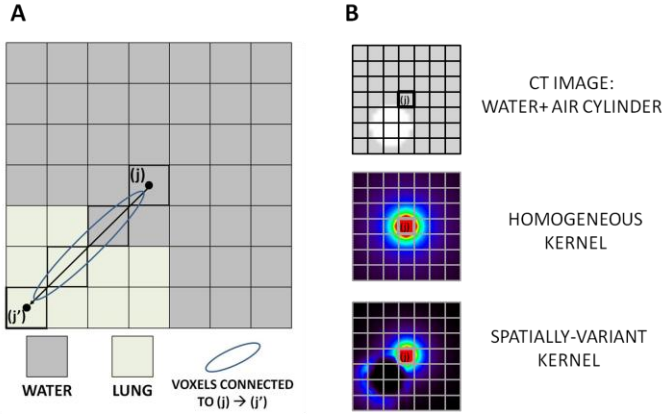

Fig. 1. A –Scheme of the procedure to obtain the spatially-variant blurring kernel in heterogeneous media. B - Comparison between the homogeneous (middle) and the spatially-variant blurring (bottom) kernels for the central voxel of the image (top).

D. Simulated phantom acquisitions

To evaluate the performance of the PR-OSEM reconstruction we used simulated phantom acquisitions in the Argus small-animal PET/CT system [34]. The simulations were performed using PeneloPET [35]. For the geometry and the electronics of the system we used the values published in [34]. We used a Monte Carlo simulation to estimate the background due to random and scatter events, and subtracted the MC-estimated background from the data [41]. A similar approach which incorporates these background counts within the reconstruction procedure can be used as well, although no significant differences are found in the resulting images [41]. The settings of each simulated phantom acquisition are summarized as follows.

D.1 - Activity concentrated in different tissues

In order to evaluate the tissue-dependent PR correction, we have simulated acquisitions of ^{18}F and ^{68}Ga line sources placed within different media:

- Water - bone phantom (Fig 2A): A water cylinder of 5 cm of diameter and 5 cm length, centered in the FOV, was simulated. It contains a 1 cm off-centered rod of bone material, 1 cm of diameter and the same length as the cylinder. Two line sources with low activity and 1 mm of diameter were simulated, placed at (1, 0, 0) cm inside water, and at (-1, 0, 0) cm inside bone, respectively. The reconstruction was performed with FIRST [42] and 100 image updates: 2 iterations of 50 subsets each of them.
- Water - lung phantom (Fig 2B): In this case we simulated a water cylinder, with 6 cm of diameter and 6 cm of length, located at the center of the FOV. Within this cylinder we simulated a lung cylinder, 1.5 cm off-centered, with 2 cm

This article has been accepted for publication in a future issue of this journal, but has not been fully edited. Content may change prior to final publication. Citation information: DOI 10.1109/TMI.2015.2436711, IEEE Transactions on Medical Imaging

of diameter and the same length than the water cylinder. Two low activity line sources were simulated, one of them placed at (1.5,0,0) cm, inside water; and the other one placed at (-1.5,0,0) cm, at the center of the lung cylinder. As in the previous case, the reconstruction was performed with FIRST [42] and 100 image updates: 2 iterations of 50 subsets each of them.

The initial activity was 2 MBq in both simulations, the energy window: 400 - 700 keV, and the number of coincidences accumulated was 20 millions. We measured the Full Width Half Maximum (FWHM) and the Full Width Tenth Maximum (FWTM) obtained in each tissue.

D.2 - Activity close to tissue boundaries (Fig. 2C)

A water cylinder (with 3.2 cm diameter and 5 cm length) was simulated at the center of the FOV with an air cylinder inside (4 mm diameter and 5 cm length and 3 mm off-centered). The activity of ^{124}I was confined in a 1 cm length line source, with a diameter of 2 mm and placed at the center of the FOV. Thus, the ^{124}I line source is situated just at the boundary between water and air. The initial activity of this line source was 2 MBq, and the number of simulated detected coincidences was 40 million counts. We set the energy window to 400 - 700 keV. This simulation was performed with and without background activity in the water volume. In the case with background activity, the simulated lesion-to-background ratio was equal to 10.

The motivation of these two simulated cases was to resemble PET imaging of rat's thyroid gland with ^{124}I [43], [44]. If the activity is placed close to the trachea, positrons can cross it and annihilate at the opposite side of the trachea. Therefore, if PR is not properly corrected artifacts will appear. Similar artifacts were reported in clinical studies [30].

In our study, we simulated the air-filled trachea as a 4 mm diameter air cylinder (Cassidy *et al* [45] reported an average tracheal diameter of 3.25±0.19 mm for rats), and the ^{124}I activity distribution as a line source of 2 mm diameter and 1 cm length. The reconstruction parameters in this case have been the same than in the previous phantoms. The reconstructions were performed with FIRST and 100 image updates: 2 iterations and 50 subsets per iteration. In order to evaluate the performance of our PR correction approaches, we measured the PET quantification in a small Volume of Interest (VOI) placed at the opposite wall of the air cylinder.

D.3 – Quantification with a simulated phantom (Fig. 2D)

For quantification purposes, we simulated a water cylinder, 3.5 cm diameter and 5.0 cm length. Within this cylinder we placed two small air cavities, centered at y = ± 1.2 cm, with 4 mm diameter and the same length than the water cylinder. A uniform activity of 10 MBq (^{124}I) is distributed in a centered cylinder with 2.0 cm diameter and 2.8 cm length. 5 small hot spheres (diameters from 3 to 5 mm) were also included in the simulation. The activity in these spheres was 4 times higher than the uniform activity in the cylinder.

In that case we measured the activity ratio in each hot sphere and the noise in the image. The errors of these estimates were obtained by weighting with the measured noise in the image.

E. Real acquisitions

The PR-OSEM reconstruction was also evaluated on phantom and mice acquisitions. The phantom acquisitions were performed at Brigham and Women's Hospital (Boston, MA) and the mice were acquired at the Instituto de Investigación Sanitaria Gregorio Marañon (Madrid, Spain) respectively. As in the simulated acquisitions, randoms and scatter corrections were performed by subtraction of the MC-estimated background counts from the measured data [41].

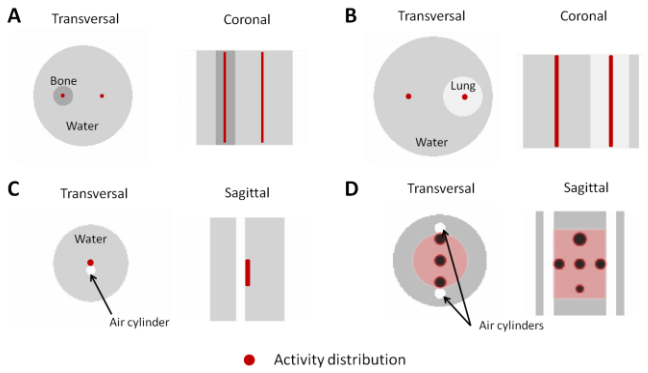

Fig. 2. Activity distribution for the four phantoms simulated in this work.

E.1 – NEMA IQ phantom

Acquisitions of a NEMA NU-4 2008 IQ phantom [46] filled with ^{124}I have been also performed in this work. The uniform region and the capillaries were filled uniformly with an activity concentration of 11.43 µCi/ml, while the hot region was filled with 52.36 µCi/ml, giving an experimental hot/background ratio of 4.58. The acquisitions were performed with an energy window of 400 – 700 keV, and reconstructed using four iterations and 20 subsets per iteration. The acquisition time was 70 minutes. We evaluated the Recovery Coefficients (RC) for the 2 and 3 mm capillaries, the contrast in the hot and cold cavities and the noise in the uniform region. The recovery coefficients, the noise and their errors were measured following the NEMA protocol for small animal tomographs [46]. The contrast values were obtained by drawing a 3D VOI of the same size and position of each cavity.

E.2 – Mouse acquisitions

Two mice, with xenografted neuroendocrine tumors , were imaged with the ^{68}Ga-DOTATOC radiotracer [47,48] in the Argus PET/CT system [34]. The injected activity was 500 µCi and 460 µCi for Mouse 1 (33 g) and Mouse 2 (32 g) respectively. The acquisitions were performed for 60 minutes after 30 minutes of uptake. with an energy window of 100 – 700 keV, and reconstructed using four iterations and 20 subsets per iteration in both cases. The segmentation of the tumor volume was performed from the PET images by drawing the 3D isocontour at 50% of the maximum pixel value. We evaluated the mean activity in the tumors relative to the mean activity in the mouse body and the standard deviation in an uniform region, located in the liver of the mouse (see Fig 7). The errors of these estimates were obtained by weighting with the measured noise in the image.

This article has been accepted for publication in a future issue of this journal, but has not been fully edited. Content may change prior to final publication. Citation information: DOI 10.1109/TMI.2015.2436711, IEEE Transactions on Medical Imaging

TABLE III. FWTM VALUES FOR THE ^{18}F AND ^{68}GA RECONSTRUCTED LINE SOURCES. IN BONE. WATER AND LUNG. AFTER THE 3D OSEM RECONSTRUCTION WITH NO PRC, WITH UNIFORM CORRECTION (ASSUMING WATER AS REFERENCE MEDIA), WITH TD AND WITH TDSV CORRECTION.

		FWTM of reconstructed line sources (mm)			
Radionuclide	**Annihilation tissue**	**No PRC**	**Unif PRC**	**TD PRC**	**TDSV PRC**
^{18}F	**Cortical bone**	1.66 ± 0.04	1.21 ± 0.03	1.37 ± 0.03	1.37 ± 0.03
	Water	1.70 ± 0.04	1.38 ± 0.04	1.38 ± 0.04	1.38 ± 0.04
	Lung	2.34 ± 0.09	1.95 ± 0.05	1.40 ± 0.04	1.40 ± 0.04
^{68}Ga	**Cortical bone**	2.60 ± 0.07	1.59 ± 0.03	1.90 ± 0.03	1.90 ± 0.03
	Water	3.24 ± 0.13	1.93 ± 0.04	1.94 ± 0.05	1.95 ± 0.04
	Lung	4.34 ± 0.26	3.22 ± 0.11	2.14 ± 0.08	2.14 ± 0.07

III. RESULTS

A. Positron range blurring kernels

Fig. 3 shows the simulated positron decay (Fig 3A) and gamma emission (Fig 3B) images for the phantom in section II.D2. The figure also shows the blurred images with TD (Fig 3C) and with TDSV (Fig 3D) blurring kernels. Fig 3E shows the profiles across the air cylinder for the previous images.

B. Simulated acquisitions

Table III shows the FWTM values for the ^{18}F and ^{68}Ga reconstructed line sources, in bone, water and lung, after the 3D PR-OSEM reconstruction with and without PR corrections. Most of the PR effects have been removed, making the FWTM obtained for ^{68}Ga more similar to that of ^{18}F .

Fig. 4 shows the results obtained for a 1 cm long ^{124}I line source near to a water-air boundary, without background activity. In that case, part of the positrons emitted by the line source may escape from the source volume, travel the 4 mm air cylinder, and annihilate at the opposite wall of this cylinder, thereby falsely suggesting activity at that location if PR effects are not appropriately corrected during reconstruction. In the upper part of the figure we plot transaxial views of the reconstructed line source, without range correction (left), with spatially-invariant (center) and with spatially-variant (right) range corrections. At the lower half we show the profiles across the line source and the air cylinder. We can see an artifact at the opposite side of the air cylinder when PR is not properly corrected. When the spatially-variant blurring kernel is employed in the reconstruction, the above mentioned artifact disappears. Table IV shows the quantification obtained in a small VOI placed at the opposite wall of the air cylinder, when no background activity was simulated. In table V we show the lesion-to-background ratios in the simulation. The background was measured within two different rois, one placed in the opposite wall of the cylinder (CYL) and the other far from the line source and the air cavity (BCK). As one can see in the table, an overestimation of background activity is observed close to the air cavity. This overestimeation is clearly reduced when using the TDSV PRC reconstruction.

Fig 5 shows the reconstructed images (with and without PR correction) for the quantification phantom. In the lower part of the figure we plot the count profiles across the 4 mm spheres and the two air cavities. We also show in table VI the ratios sphere/uniform for each sphere and the activity ratios (versus mean activity in a uniform region) for the VOI in the opposite walls of the two air cylinders. These values were obtained at a level of noise of approximately 10%, that is after 280 image updates in the reconstruction without PR correction, and 100 image updates in the TD and TDSV reconstructions.

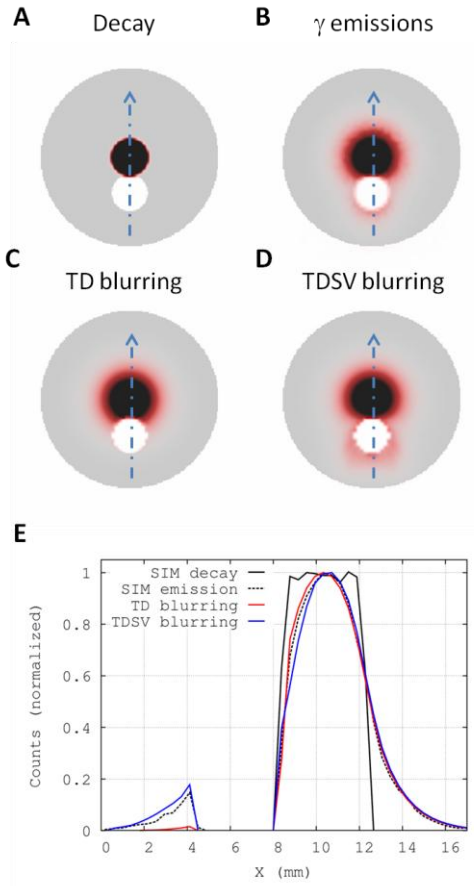

Fig. 3. A & B: PeneloPET simulation of the positron decay (A) and gamma-ray emission (B) positions for the phantom in section II.D2. C & D: Decay image blurred by using the homogeneous (C), and spatially-variant (D), tissue-dependent blurring kernels implemented in this work. In panel E we show the normalized count profiles, across the air cylinder, for the two blurring kernels and the simulated decay and emission images.

This article has been accepted for publication in a future issue of this journal, but has not been fully edited. Content may change prior to final publication. Citation information: DOI 10.1109/TMI.2015.2436711, IEEE Transactions on Medical Imaging

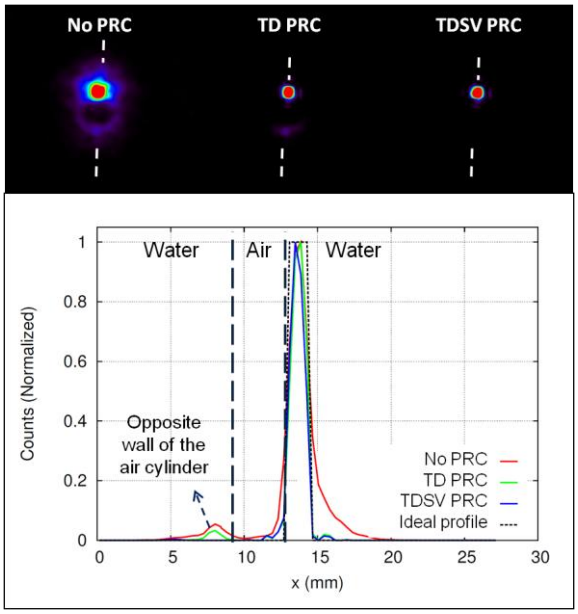

Fig. 4. Top: transverse views of the line source reconstructed with the PR-OSEM procedure without range correction (left), spatially-invariant (center) and spatially-variant (right) positronrange corrections. Bottom: Activity profiles across the source and the air cylinder for the three reconstructed images.

TABLE IV. RESIDUAL ACTIVITY SEEN IN THE OPPOSITE WALL OF THE CYLINDER (SEE FIGURE 4) VS THE MEAN ACTIVITY IN THE SOURCE (IN PERCENTAGE).

	No PRC	TD PRC	TDSV PRC
Ratio air cylinder (%)	5.88 ± 0.31	3.29 ± 0.23	0.0020 ± 0.0004

TABLE V. LESION-TO-BACKGROUND RATIO FOR THE ^{124}I LINE SOURCE WITH AN UNIFORM BACKGROUND ACTIVITY. THE BACKGROUND WAS MEASURED IN THE OPPOSITE WALL OF THE CYLINDER (CYL) AND FAR FROM THE LINE SOURCE AND THE AIR CAVITY (BCK). THE THEORETICAL VALUES ARE REPRESENTED IN THE TABLE AS "EXP".

	Lesion-to-background Ratio			
	No PRC	**TD PRC**	**TDSV PRC**	**EXP**
BCK	5.26 ± 0.05	9.02 ± 0.14	9.46 ± 0.14	10.0
CYL	3.88 ± 0.10	6.89 ± 0.23	9.06 ± 0.04	10.0
Overestimation (%)	35.4 ± 4.8	31.0 ± 2.3	4.4 ± 2.1	0.0

TABLE VI. RATIOS SPHERE/UNIFORM FOR EACH SPHERE IN THE PHANTOM AND ACTIVITY RATIOS IN THE TWO OPPOSITE WALLS OF THE AIR CYLINDERS, AT THE SAME LEVEL OF NOISE. THE THEORETICAL VALUES ARE REPRESENTED IN THE TABLE AS "EXP".

ROI	**Ratio ROI/Uniform (Noise ~ 10%)**			
	No PRC	**TD PRC**	**TDSV PRC**	**EXP**
S1 (4 mm)	2.08 ± 0.13	3.6 ± 0.4	4.0 ± 0.5	4.0
S2 (4 mm)	1.64 ± 0.10	2.7 ± 0.3	3.0 ± 0.3	
S3 (4 mm)	1.54 ± 0.10	3.1 ± 0.4	3.6 ± 0.4	
S4 (5 mm)	1.66 ± 0.11	3.6 ± 0.4	4.0 ± 0.5	
S5 (3 mm)	1.42 ± 0.09	2.3 ± 0.3	2.5 ± 0.3	
Artifact1	0.149 ± 0.008	0.21 ± 0.02	0.081 ± 0.009	0.0
Artifact2	0.087 ± 0.005	0.112 ± 0.013	0.023 ± 0.003	

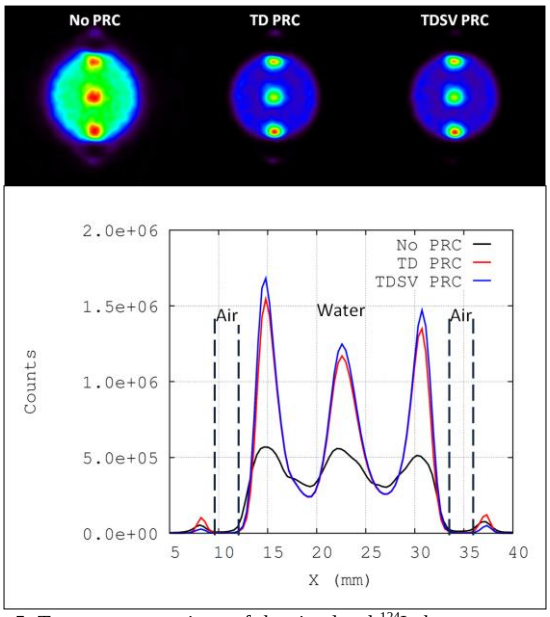

Fig. 5. Top: transverse views of the simulated ^{124}I phantom reconstructed with the PR-OSEM procedure without PR correction (left), spatially-invariant (center) and spatially-variant (right) PR corrections. Bottom: Activity profiles for the three reconstructed images.

C. Phantom and mouse acquisitions

The transversal and coronal images (with and without range correction) obtained from the NEMA IQ acquisitions are represented in Fig 6. In table VII we present the RC values, the contrast for the hot and cold regions and the noise in the image obtained without, with tissue-dependent and with spatially-variant PR correction. These values were obtained at the same level of noise, after 160 (No PRC) and after 100 (TD and TDSV) image updates. The resolution and contrast of the images is significantly improved when PRC is applied. Finally, we show in Fig 7 the transversal and coronal views of one of the studied mice, reconstructed without and with PR correction. The tumor segmentation and the VOI in a uniform region are also shown. The count profiles across the tumor are also represented in the figure. Table VIII shows the quantification obtained in the tumor for the two mice and the measured noise in the uniform region. As in the previous cases, these values correspond to the same noise level, and were obtained from reconstructions with 260 (No PRC) and 100 (TD and TDSV) image updates.

TABLE VII. CONTRAST IN THE HOT AND COLD REGIONS OF THE IQ PHANTOM. RECOVERY COEFFICIENTS FOR THE 2, 3, 4 AND 5 MM CAPILLARIES AND NOISE IN THE UNIFORM REGION. THE THEORETICAL VALUES ARE REPRESENTED AS "EXP".

	No PRC	**TD PRC**	**TDSV PRC**	**EXP**
Hot/BCKG	3.6 ± 0.5	4.6 ± 0.6	4.6 ± 0.6	4.6
Cold/BCKG	0.16 ± 0.02	0.09 ± <0.01	0.10 ± <0.01	0.0
RC (2 mm)	0.27 ± 0.08	0.6 ± 0.2	0.6 ± 0.2	1.0
RC (3 mm)	0.50 ± 0.14	1.3 ± 0.5	1.3 ± 0.5	1.0
RC (4 mm)	0.51 ± 0.17	1.2 ± 0.4	1.2 ± 0.4	1.0
RC (5 mm)	0.63 ± 0.17	1.2 ± 0.4	1.2 ± 0.4	1.0
Noise (%)		~16 ± 1 %		-

This article has been accepted for publication in a future issue of this journal, but has not been fully edited. Content may change prior to final publication. Citation information: DOI 10.1109/TMI.2015.2436711, IEEE Transactions on Medical Imaging

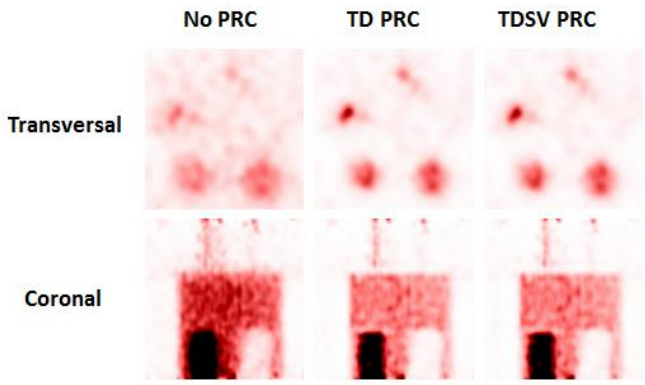

Fig. 6. Transversal and coronal slices of the reconstructed IQ phantom filled with ^{124}I. Reconstruction without PR correction (left), with tissue-dependent correction (center) and with spatially-variant correction (right).

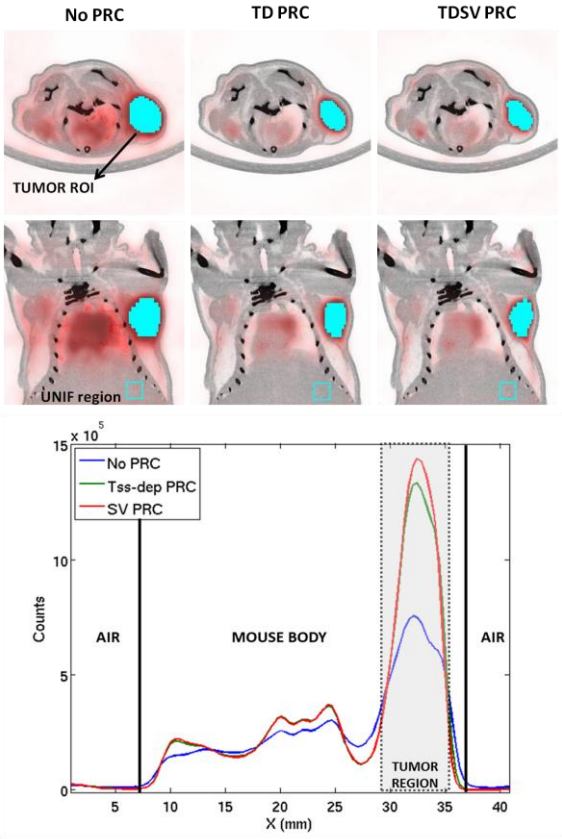

Fig. 7. Top: transversal and coronal PET/CT images without range corrections (left), with tissue dependent correction (center) and with spatially-variant correction (right) of a mouse injected with ^{68}Ga. Bottom: count profiles across the mouse tumor for the cases under study. All images were corrected by attenuation, scatter and random coincidences.

We see a significant reduction of the apparent tumor size when PRC is applied, because of the higher resolution of the range-corrected images. We also notice a better localization of the activity in the range-corrected images, with almost no activity in regions in which not activity should be seen (as for example in the lungs or in the air surrounding the mice bodies).

TABLE VIII. TUMOR/MOUSE RATIO ACTIVITIES AND NOISE IN A UNIFORM REGION, MEASURED IN IMAGES RECONSTRUCTED WITHOUT RANGE CORRECTION, WITH TD AND WITH TDSV RANGE CORRECTIONS. THE ROIS FOR THE TUMOR AND THE UNIFORM REGION ARE DEPICTED IN FIGURE 7.

	Mouse 1		Mouse 2	
	Tumor/ MOUSE	%SD (UNIF)	Tumor/ MOUSE	%SD (UNIF)
No PRC	4.5 ± 0.6	13.2 ± 0.2	4.2 ± 0.5	13.0 ± 0.2
TD PRC	8.1 ± 0.3	12.4 ± 0.2	7.6 ± 0.2	12.4 ± 0.2
TDSV PRC	8.6 ± 0.3	12.8 ± 0.2	8.3 ± 0.3	12.6 ± 0.2

D.Reconstruction time

Table IX shows the reconstruction time for one of the mice in section III.C, reconstructed without PR correction, with tissue-dependent and with spatially-variant corrections. In the cases with PR correction, we compared the overhead in reconstruction time due to different sizes of the blurring kernel, from short-range radionuclides (^{18}F) to medium and large range radionuclides (^{68}Ga and ^{124}I). As expected, the kernel size, and in consequence the overhead in reconstruction time, increases with the spatial extent of the PR.

In all cases the reconstructions were performed on a 3.0 GHz Intel(R) Xeon(R) 64 bit CPU. The results were obtained with two iterations, 50 subsets per iteration, and in a single thread application. For the TDSV correction, we also implemented an openMP parallelization for the computation of the blurring kernel and for the blurring operation. We show in the table the computation time for an 8 threads execution of the TDSV correction.

TABLE IX. RECONSTRUCTION TIME FOR MOUSE 1 (SECTION III.C) USING DIFFERENT KERNELS FOR PR CORRECTION AND RECONSTRUCTION METHODS.THE RECONSTRUCTIONS WERE PERFORMED IN A SINGLE CORE BY USING 2 ITERATIONS AND 50 SUBSETS PER ITERATION, EXCEPT FOR THE TDSV METHOD, WHERE WE ALSO EVALUATED A PARALLEL IMPLEMENTATION IN 8 CORES.

Kernel used for PRC	Intel Xeon @ 3.00GHz - 2 IT / 50 SS			
	Single thread			8 threads
	No PRC	TD PRC	TDSV PRC	TDSV PRC
^{18}F	6 m 7 s	6 m 28 s	7 m 21 s	6 m 31 s
^{68}Ga	6 m 7 s	15 m 35 s	55 m 36 s	9 m 30 s
^{124}I	6 m 7 s	19 m 34 s	74 m 42 s	12 m 45 s

IV. DISCUSSION

The proposed methods for PR correction improve significantly the image quality when using medium-large range radionuclides (see Fig. 4 to 8). In this work we presented, as reference, images obtained with ^{68}Ga and ^{124}I radionuclides. Nevertheless, similar results were obtained for the other medium-large range radionuclides modeled in this work (^{13}N, ^{15}O, ^{94m}Tc, ^{82}Rb, ^{76}Br and ^{86}Y).

The PR modelling for all the radionuclides was performed by using the PeneloPET Monte Carlo code [35]. The accuracy of the model was evaluated in [15] by comparison with other published experimental and simulated results, giving consistent results, with errors below 10% in the majority of the

This article has been accepted for publication in a future issue of this journal, but has not been fully edited. Content may change prior to final publication. Citation information: DOI 10.1109/TMI.2015.2436711, IEEE Transactions on Medical Imaging

cases. As we have demonstrated in [25], an error below 10% in the modelling of the PR employed for acquisition simulation and image reconstruction has a negligible effect on the reconstructed images. The scaling method to estimate the PR distributions for any tissue, given the distribution in water, was confirmed according to PeneloPET simulations. Scaling by the electronic density of media has been shown to work well, with excellent accuracy in all the cases [15,16].

In order to obtain reliable PRC images, a PR correction dependent on the annihilation tissue is necessary. For example, in table 3 we show the FWTM of reconstructed line sources placed in different media (water, bone and lung). If we perform uniform PR correction (taken the PR profiles in water only) the line source placed in the bone region is over-corrected and shows a very high peak of the activity profiles. We also see an under-correction when the line source is placed in lung. When tissue-dependent PR is modeled into the reconstruction, similar apparent sizes for the line sources and identical height of the activity profiles are obtained for the three tissues.

The tissue-dependent (TD) correction works well in most cases, except when the activity is placed close to a tissue-boundary (see figures 4 and 5). In that case, the tissue-dependent but spatially-invariant blurring kernel used by the TD correction does not represent well the 3D positron annihilation distribution, which is naturally anisotropic (see figure 3). For these cases, we implemented a tissue-dependent and spatially-variant (TDSV) PR correction algorithm. The TDSV blurring kernel is more similar to the simulated 3D annihilation distribution, as shown in figure 3. It is no surprise that the TDSV correction produced the best images. TDSV reconstruction, however, are not widely used due to the large computation penalty that may involve. In this work we took advantage of the good scaling of PR in different materials by the density of said materials, in order to implement a tissue variant blurring kernel fully incorporating PR effects in different materials. Although the profiles of the TDSV blurring in figure 3 show a slight overestimation near the air cavity, this overcompensation has not a significant effect in the reconstructed images, as we can see in figures 4 and 5 and in tables IV and V. This is anyway expected, giving the fact that inaccuracies below 10% in the blurring kernels, as it is the case in the TDSV kernels, result in not significant differences in the PRC images [25].

As we can see in tables VI and VII, the TDSV range correction further improves the quantification of lesions of interest, giving activity-ratio values closer to the theoretical ones, both in simulations and in real acquisitions. As expected, the noise in the image increases when PR correction is applied, due to the de-blurring procedure used for correcting the range blurring effect.

Note that the RC values for the 3, 4 and 5 mm capillaries in table VII are slightly higher than the theoretical values in both TD and TDSV reconstructions. This over-estimation of activities is due to small "Gibbs" artifacts [49-51] introduced by the range correction procedure. It is also noticeable the high level of noise in these IQ images. The noise affects the accuracy of the RC values and causes an over-estimation of them. These Gibbs artifacts and excess of noise could be corrected for by using a stopping rule of the iterative algorithm or performing a Gaussian post-filtering of the images. We preferred not to follow any of these approaches in order to conserve the high-resolution properties of the range-corrected images.

Finally, and regarding the mice studies, we have observed that the quantification of tumors improves significantly when PR correction is incorporated into the reconstruction algorithm (table VIII). Better quantification and delimitation of tissue boundaries is obtained when the TDSV correction is applied instead of just TD correction (Fig. 7).

As seen in table IX, the computation of the TDSV blurring kernel adds a manageable overhead to the overall reconstruction time, comparing with the TD correction. For the larger range radioisotopes, full spatial variant range requires 4 times longer computation times for long range isotopes. Even though, less than 80 minutes of reconstruction for the worst case can be considered a good starting point for real world applications. Most of the overhead is due to the precomputation of the kernel from the CT image, and this needs to be done only once, even for dynamical multiframe images. Furthermore, the implementation of positron range we devise in this work allows for straightforward parallelization and the use of a large number of subsets, as it is based on the FIRST code which allows up to 100 subsets per iteration, and can be implemented to use multi-core and multi-cpu execution or in the GPU with significant speed-ups [52]. Adding two simple openMP directives in the precomputation and positron range blurring sections yields a multi-core version of the TDSV algorithm performing six times faster using 8 threads of an already common quad-core cpu, yielding the total reconstruction time back to a few minutes even for the largest positron range case.

The proposed methods for PR correction could be applied to any other PET system, provided an accurate modeling of the PR and the System Response Matrix (without range effects) of the system are available. These methods can also be used to improve the quantification accuracy in clinical PET imaging with large range radionuclides, such as cardiac imaging with ^{82}Rb [4] or thyroid imaging using ^{124}I [30]. Furthermore, our TD and TDSV range corrections can be easily applied in presence of magnetic fields (PET/MR systems), provided an accurate 3D modeling of the PR kernel in the magnetic field (which will be naturally anisotropic), as the one performed by Kraus *et al* [26].

V. Conclusion

We have implemented an accurate and efficient spatially-variant PR correction, which yields artifact-free reconstructed images when the activity is placed close to tissue-boundaries or in heterogeneous media. It is possible to improve significantly the quality of the reconstructed images for medium-large PR radionuclides, like ^{124}I or ^{68}Ga, when range corrections are taken into account. While in most cases the TD PRC shows results good enough with a very small

This article has been accepted for publication in a future issue of this journal, but has not been fully edited. Content may change prior to final publication. Citation information: DOI 10.1109/TMI.2015.2436711, IEEE Transactions on Medical Imaging

performance penalty compared to the no range correction version, the availability of a fast implementation on parallelized multi-core approaches of the TDSV PRC is an attractive alternative for producing higher quality PET images.

ACKNOWLEDGMENT

We acknowledge Dr. Eduardo Lage, Prof. Stephen C. Moore and Dr. Mi-Ae Park for the acquisition of the Image Quality phantom (section II-E.1). We also acknowledge Drs M. Soto-Montenegro and S. Peña for providing access to the animals and the tracers, and A. de Francisco and Y. Sierra for their skilful support during the imaging sessions.

REFERENCES

[1] S. Vallabhajosula, L. Solnes and B. Vallabhajosula, "A Broad Overview of Positron Emission Tomography Radiopharmaceuticals and Clinical Applications: What Is New?", *Semin Nucl Med*, vol 41, pp 246-264, 2011.

[2] C.S. Levin and E.J. Hoffman, "Calculation of positron range and its effect on the fundamental limit of positron emission tomography system spatial resolution", *Phys. Med. Biol.*, vol 44, pp 781-799, 1999.

[3] J. Cal-Gonzalez, J. L. Herraiz, S. España, M. Desco, J. J. Vaquero, and J. M. Udías. "Positron range effects in high resolution 3D PET imaging", in *IEEE NSS-MIC Conference Record*, 2009, pp 2788-2792.

[4] A. Rahmim, J. Tang, M. A. Lodge, S. Lashkari, M. R. Ay, R. Lautamäki, B. M. W. Tsui, and F. M. Bengel, "Analytic system matrix resolution modeling in PET: An application to Rb-82 cardiac imaging", *Phys. Med. Biol.*, vol 53, pp 5947-5965, 2008.

[5] V. Y. Panin, F. Kehren, C. Michel, and M. Casey, "Fully 3D PET reconstruction with system matrix derived from point source measurements", *IEEE Trans. Med. Imaging*, vol 25, no. 7, pp 907-921,2006.

[6] J. R. Stickel and S. R. Cherry, "High-resolution PET detector design: Modeling components ofintrinsic spatial resolution", *Phys. Med. Biol.*, vol 50, pp 179-195, 2005.

[7] J. Qi, R. M. Leahy, S. R. Cherry, A. Chatziioannou, and T. H. Farquhar. "High-resolution 3D Bayesian image reconstruction using the microPET small-animal scanner", *Phys. Med. Biol.*, vol 46, pp 2597-2605, 1998.

[8] S. Derenzo, "Measurement of annihilation point spread distribution for medically importantpositron emitters", In *5th Int. Conf. of Positron Annihilation*, pp 819-823, 1979.

[9] M. E. Phelps, E. J. Hoffman, and S. Huang, "Effects of Positron Range on Spatial Resolution", *J. Nucl. Med*., vol 16, pp 649-652, 1975.

[10] Z. H. Cho, J. K. Chan, L. Ericksson, M. Singh, S. Graham, N. S. Macdonald, and Y. Yano, "Positron Ranges Obtained From Biomedically Important Positron-Emitting Radionuclides", *J. Nucl. Med*., vol 16, pp 1174-1176, 1975.

[11] M. R. Palmer, X. Zhu, and J. A. Parker, "Modeling and Simulation of Positron Range Effects for High Resolution PET Imaging", *IEEE Trans. Nucl. Sci.*, vol 52, pp 1391-1395, 2005.

[12] M. R. Palmer and G. L. Brownell, "Annihilation density distribution calculations for medically important positron emitters", *IEEE Trans. Med. Imaging*, vol 11, pp 373-378, 1992.

[13] P. D. Olcott, E. Gonzalez, A. Vandenbroucke and C. S. Levin, "Mixture model for fast estimation of positron range", In *IEEE NSS-MIC Conference Record*, pp 3058-60, 2010.

[14] A. Eleftheriou, C. Tsoumpas, O. Bertolli, E. Stiliaris, "Effect of the magnetic field on positron range using GATE for PET-MR", *EJNMMI Physics*, vol 1(S1): A50, 2014.

[15] J. Cal-González, J. L. Herraiz, S. España, P. M. G. Corzo, M. Desco, J. J. Vaquero, and J. M. Udías, "Positron Range Estimations with PeneloPET", *Phys. Med. Biol.*, vol 58, pp 5127-5152, 2013.

[16] L. Jødal, C. Le Loirec, and C. Champion, "Positron range in PET imaging: an alternativeapproach for assessing and correcting the blurring", *Phys. Med. Biol*., vol 57, pp 3931-3943, 2012.

[17] W. Lehnert, M. C. Gregoire, A. Reilhac, and S. R. Meikle, "Analytical positron range modelling in heterogeneous media for PET Monte Carlo simulation", *Phys. Med. Biol.*, vol 56, pp 3313-35, 2011.

[18] C. Champion and C. Le Loirec, "Positron follow-up in liquid water: II. spatial and energetic study for the most important radioisotopes used in PET", *Phys. Med. Biol*., vol 52, pp 6605-6625, 2007.

[19] C. Le Loirec and C. Champion, "Track structure simulation for positron emitters of medical interest. Part I: The case of the allowed decay isotopes", *Nucl. Inst. Meth. in Phys. Res. A*, vol 582, pp 644-653, 2007.

[20] C. Le Loirec and C. Champion, "Track structure simulation for positron emitters of physical interest. Part II: The case of the radiometals", *Nucl. Inst. Meth. in Phys. Res. A*, vol 582, pp 654-664, 2007.

[21] C. Le Loirec and C. Champion, "Track structure simulation for positron emitters of physical interest. Part III: The case of the non-standard radionuclides", *Nucl. Inst. Meth. in Phys. Res. A*, vol 582, pp 665-672, 2007.

[22] A. Sánchez-Crespo, P. Andreo, and S. A. Laarson, "Positron flight in human tissues and its influence on PET image spatial resolution", *Eur. J. Nucl. Med. Mol. Imaging*, vol 31, pp 44-51, 2004.

[23] R. L. Harrison, M. S. Kaplan, S. D. Vannoy, and T. K. Lewellen, "Positron range and coincidencenon-collinearity in SimSET", In *IEEE NSS-MIC Conference Record*, pp 1265-1268, 1999.

[24] S. E. Derenzo, "Mathematical Removal of Positron Range Blurring in High Resolution Tomography", *IEEE Trans. Nucl. Sci.*, vol 33, pp 565-569, 1986.

[25] J. Cal-González, J. L. Herraiz, S. España, E. Vicente, E. Herranz, M. Desco, J. J. Vaquero, and J. M. Udías, "Study of CT-based positron range correction in high resolution 3D PET Imaging", *Nucl. Inst. Meth. in Phys. Res. A*, vol 648, pp S172-S175, 2011.

[26] R. Kraus, G. Delso, and S. I. Ziegler, "Simulation Study of Tissue-Specific Positron Range Correction for the New Biograph mMR Whole-Body PET/MR System", *IEEE Trans. Nucl. Sci.*, vol 59, pp 1900-1909, 2012.

[27] O. Bertolli, M. Cecchetti, N. Camarlinghi, A. Eleftheriou, N. Belcari, C. Tsoumpas, "Iterative reconstruction incorporating positron range correction within STIR framework", *EJNMMI Physics*, vol 1(S1): A42, 2014.

[28] B. Bai, R. Laforest, A. M. Smith, and R. M. Leahy, "Evaluation of MAP image reconstruction with positron range modeling for 3D PET", In IEEE NSS-MIC Conference Record, pp 2686-2689, 2005.

[29] B. Bai, A. Ruangma, R. Laforest, Y. C. Tai, and R. M. Leahy, "Positron range modeling for statistical PET image reconstruction", In *IEEE NSS-MIC Conference Record*, pp 2501-2505, 2003.

[30] S. B. Abdul-Fatah, M. Zamburlini, S. G. E. A. Halders, B. Brans, G. J. J. Teule, and G. J. Kemerink, "Identification of a

Shine-Through Artifact in the Trachea with 124I PET/CT", *J Nucl Med*, vol 50, pp 909-911, 2009.

[31] A. Alessio and L. MacDonald, "Spatially Variant Positron Range Modeling Derived from CT for PET Image Reconstruction", In *IEEE NSS-MIC Conference Record*, pp 2912-2915, 2009.

[32] M. Moreau, I. Buvat, L. Ammour, N. Chouin, F. Kraeber-Bodéré, M. Chérel and T. Carlier, "Assessment of a fully 3D Monte Carlo reconstruction method for preclinical PET with iodine-124", *Phys. Med. Biol.* Vol 60, pp 2475-2491, 2015.

[33] L. Fu and J. Qi, "A residual correction method for high-resolution PET reconstruction with application to on-the-fly Monte Carlo based model of positron range", *Med. Phys*., vol 37, pp 704-714, 2010.

[34] Y. Wang, J. Seidel, W. M. B. Tsui, J. J. Vaquero, and M. G. Pomper, "Performance Evaluationof the GE Healthcare eXplore VISTA Dual-Ring Small-Animal PET Scanner", *J. Nucl. Med.*, vol 47, pp 1891-1900, 2006.

[35] S. España, J. L. Herraiz, E. Vicente, J. J. Vaquero, M. Desco, and J. M. Udías, "PeneloPET, a Monte Carlo PET simulation tool based on PENELOPE: features and validation", *Phys. Med. Biol.*, vol 54, 1723-1742, 2009.

[36] J Baró, J Sempau, J M Fernández-Varea and F. Salvat, "PENELOPE: an algorithm for Monte Carlo simulation of the penetration and energy loss of electrons and positrons in matter", Nucl. *Instrum. Methods Phys. Res. B*, vol 100, 31–46, 1995.

[37] F Salvat, J M Fernández-Varea and J. Sempau, "PENELOPE-2008: A code system for Monte Carlo simulation of electron and photon transport", NEA No. 6416, Organisation For Economic Co-Operation And Development, 2008.

[38] E. N. Tsyganov et al, Small-Animal SPECT Imaging, chapter "Reconstruction Algorithm with Resolution Deconvolution in a Small-Animal PET Imager". Springer, New York, 2005. ISBN978-0-387-25143-1.

[39] G. L. Zeng and G. Y. Gullberg, "Unmatched projector/backprojector pairs in an iterative reconstruction algorithm", *IEEE Trans.Med. Imaging*, vol 19, pp 548-555, 2000.

[40] G. L. Zeng, G. Y. Gullberg, B. M. W. Tsui, and J. A. Terry, "Three-dimensional iterative reconstruction algorithms with attenuation and geometric point response correction", *IEEE Trans. Nucl. Sci*., vol 38, pp 693-702, 1991.

[41] J. Cal-Gonzalez, S. C. Moore, M.-A. Park, J. L. Herraiz, J. J. Vaquero, M. Desco and J. M. Udias, "Improved quantification for local regions of interest in PET", submitted to: *Phys. Med. Biol.*

[42] J. L. Herraiz, S. España, J. J. Vaquero, M. Desco, and J. M. Udías, "FIRST: Fast Iterative Reconstruction Software for (PET) tomography", *Phys. Med. Biol*., vol 51, pp 4547-4565, 2006.

[43] M. Emanuelsson. "Development of an animal in vivo 124I-MicroPET/MicroCAT imaging model of the thyroid", Master's thesis, Lund University, 2006.

[44] Y. Kanai, N. Takahashi, T. Watabe, H. Watabe, S. Yamamoto, E. Shimosegawa, A. Shinohara, K. Nakai, and J. Hatazawa, "Rat thyroid gland imaging with 124I using semiconductor PET scanner and PET-MR", *J. Nucl. Med*., vol 53 (S1), pp 1221, 2012.

[45] K. J. Cassidy, J. L. Bull, M. R. Glucksberg, C. A. Dawson, S. T. Haworth, R. Hirschl, N. Gavriely and J. B. Grotberg, "A rat lung model of instilled liquid transport in the pulmonary airways", *J. Appl. Physiol*., vol 90, pp 1955-1967, 2001.

[46] NEMA-NU-4. Performance Measurements for Small Animal Positron Emission Tomographs.Technical report, National Electrical Manufacturers Association, 2008.

[47] T. D. Poeppel, I. Binse, S. Petersenn, H. Lahner, M. Schott, G. Antoch, W. Brandau, A. Bockisch and C. Boy, "^{68}Ga-DOTATOC Versus ^{68}Ga-DOTATATE PET/CT in Functional Imaging of Neuroendocrine Tumors", *J Nucl Med*, vol. 52(12), pp 1864-1870, 2011.

[48] M. L. Soto-Montenegro, S. Peña-Zalbidea, J. M. Mateos-Pérez, M. Oteo, E. Romero, M. A. Morcillo and M. Desco, "Meningiomas: A Comparative Study of ^{68}Ga-DOTATOC, ^{68}Ga-DOTANOC and ^{68}Ga-DOTATATE for Molecular Imaging in Mice", *PLoS ONE*, vol 9 (11), pp e111624. 2014.

[49] D. L. Snyder, M. I. Miller, L. J. Thomas, and D. G. Politte, "Noise andedge artifacts in maximum-likelihood reconstruction for emission tomography," *IEEE Trans. Med. Imaging*, vol 6, pp 228–238, 1987.

[50] S. Tong, A. M. Alessio, K. Thielemans, C. Stearns, S. Ross, andP. E. Kinahan, "Properties and mitigation of edge artifacts in PSF-based PET reconstruction", *IEEE Trans. Nucl. Sci.*, vol 58(5), pp 2264–2275, 2011.

[51] A. Rahmim, "Resolution modeling in PET imaging: Theory, practice, benefits, and pitfalls", *Med. Phys.*, vol 40(6), 064301, 2013.

[52] J. L. Herraiz, S. España, J. Cal-González, J. J. Vaquero, M. Desco, and J. M. Udías, "Fully 3D GPU PET reconstruction", *Nucl. Instrum. Meths. Phys. Res. A*, vol 648, pp S169-S171, 2011.